Advances in Science and Technology Research Journal

Advances in Science and Technology Research Journal, 2026, 20(6), 422–444
https://doi.org/10.12913/22998624/218215
ISSN 2299-8624, License CC-BY 4.0

Received: 2025.11.17
Accepted: 2026.04.15
Published: 2026.05.01

Design, analysis, and performance evaluation of a bladeless vibration-based piezoelectric energy-harvesting wind turbine

Naseer Ahmad[1*], Muhammad Jawad Rafique[1], Ammad Ejaz[1]

[1] Department of Mechanical Engineering, University of Engineering and Technology, Lahore, 39161, Pakistan
* Corresponding author's e-mail: nahmad@uet.edu.pk

ABSTRACT

This study investigates a bladeless wind turbine concept that converts wind-induced structural vibrations into electrical energy through piezoelectric transduction. Three prototype configurations with different bluff body geometries (cube, cylinder, and sphere) mounted on elastic masts were designed and tested. Computational simulations including computational fluid dynamics (CFD) for aerodynamic forces and finite-element modal and harmonic analyses in ANSYS were performed. Wind tunnel experiments at 6.94 m/s (25 km/h) were also conducted to measure prototype voltage output. CFD analysis provided drag, lift, and axial forces for each geometry, while modal analysis identified natural frequencies and mode shapes. A piezoelectric transducer was bonded to the mast at the location of maximum deformation predicted by the third bending mode. Harmonic response simulations estimated the voltage output, which was validated against experimental measurements. Results showed that the cube-tipped mast produced the highest open-circuit voltage (~5 mV), followed by the cylinder (4 mV) and the sphere (3 mV) at 6.94 m/s. The sphere-tipped design demonstrated the lowest drag and voltage output. Numerical simulations from ANSYS closely matched the experimental results, confirming the reliability of the coupled CFD–FEA approach. Overall, the findings demonstrated the feasibility of bladeless wind energy harvesters and highlighted the influence of bluff body geometry on aerodynamic forces, structural response, and harvested power. These results provide a foundation for optimizing piezoelectric wind harvesters toward higher efficiency and practical deployment.

Keywords: piezoelectric energy harvesting, bladeless wind turbine, vibration-based energy harvesting, flow-induced vibrations, vortex-induced vibration, computational fluid dynamics, finite element analysis.

INTRODUCTION

Harvesting wind energy using bladeless, vibration-based turbines offers a promising alternative to conventional rotary turbines [1, 2]. Unlike traditional bladed turbines, which involve high maintenance, noise, and ecological hazards (e.g., bird and bat strikes), bladeless systems rely on flow-induced vibrations of a structural element, eliminating complex moving parts [3, 4]. The oscillatory motion of these structures can be converted into usable electrical energy through piezoelectric materials. Piezoelectric materials convert mechanical strain into electrical charge (direct effect) [5] and deform under applied electric fields (converse effect) as illustrated in Figure 1. This dual functionality, combined with high electromechanical efficiency and scalability to the micro/nanoscale, makes them essential for modern sensing, actuation, and energy-harvesting technologies [6, 7]. and has made them central to modern energy and sensor systems.

In recent years, the unique properties of piezoelectric materials have been widely exploited in micro- and nano-electromechanical systems (MEMS/NEMS). Their dual characteristics make them highly versatile for sensing and actuation in microsystems, offering precise control and self-powered operation. Importantly, piezoelectric transducers deliver high electromechanical energy conversion efficiency and remain effective even as device dimensions shrink, providing

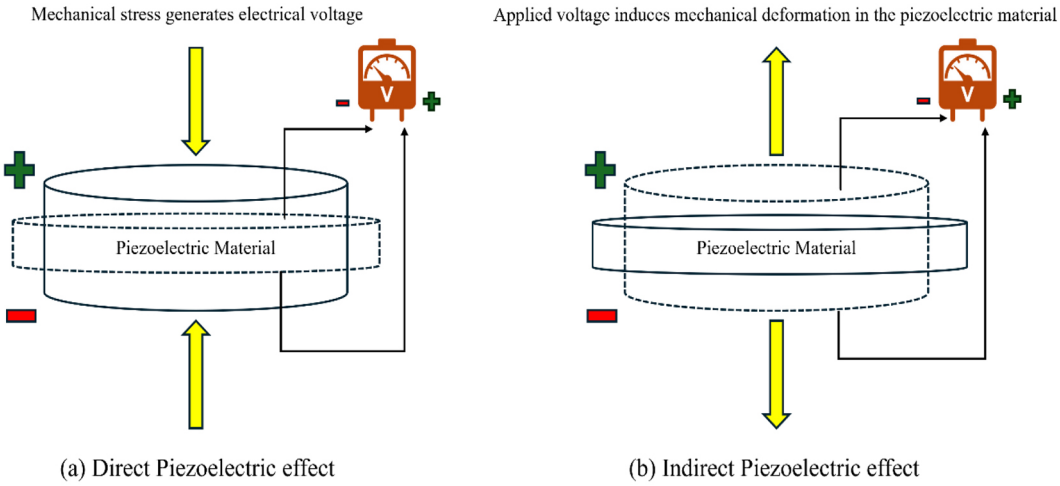

(a) Direct Piezoelectric effect (b) Indirect Piezoelectric effect

Figure 1. Illustration of the piezoelectric effect: (a) direct effect – mechanical stress generates electrical voltage, (b) indirect effect – applied voltage induces mechanical deformation in the piezoelectric material

superior scalability compared with electrostatic actuators, whose force output decreases significantly with miniaturization [8, 9].

The integration of piezoelectric thin films onto silicon or flexible substrates has enabled the fabrication of micro-sensors with high sensitivity and wide dynamic range, eliminating the need for external power to generate signals [10–12]. For example, piezoelectric MEMS pressure sensors and accelerometers can produce measurable charges in response to very small stimuli, reducing reliance on power-intensive amplification and enabling true self-powered operation [11]. On the actuation side, piezoelectric devices achieve high precision, fast response, and significant force or displacement relative to their small size [13–16]. MEMS piezo actuators such as piezoelectric micromirrors and micro-positioners, offer nanometer-scale motion control with bandwidths spanning kHz to MHz, far exceeding the performance of thermal or magnetic counterparts [17].

Beyond sensing and actuation, piezoelectric materials are also attractive for micro-power generation because of their strong electromechanical coupling and high energy density [18–20]. Piezoelectric MEMS energy harvesters can convert ambient vibrations or biomechanical motion into electricity [21, 22], providing compact and cost-effective solutions for scavenging wasted environmental energy [23, 24]. These characteristics make piezoelectric materials particularly well suited for vibration-based energy harvesting, including wind-induced oscillations where structural motion is directly converted into electrical output. Recent decades have seen growing interest in harnessing flow-induced vibrations for power generation. Vortex-induced vibration (VIV) harvesters are among the most studied configurations. In a VIV harvester, a bluff body (e.g. a cylinder) in a flow sheds vortices alternately from its sides, creating an oscillatory transverse force. When the vortex shedding frequency (f_s) coincides or nearly coincides with one of the structure's natural frequencies (f_n), a lock-in phenomenon occurs, resulting in large-amplitude synchronized oscillations. Sarpkaya (2004) provides a critical review of the VIV mechanism, explaining how the intrinsic fluid-structure coupling leads to lock-in and how parameters like Reynolds number and body shape affect the vibration amplitude [25]. In essence, the shed vortices impart periodic forces at frequency $f_s = St \times (U/D)$, where St is the Strouhal number, U the flow speed, and D a characteristic dimension of the bluff body. As the flow speed varies, f_s may pass through f_n, triggering resonance.

Flexible structures with attached piezoelectric elements can convert these oscillations into electrical energy. Akaydın et al. (2010) demonstrated this by placing a piezoelectric polymer beam in the wake of a cylinder; the beam's oscillations generated an AC voltage, but only within a narrow bandwidth around resonance [26]. In subsequent wind tunnel experiments, Akaydin et al. (2012) varied the flow speed and observed the performance of a self-excited piezoelectric harvester, noting that maximum power output occurs in the lock-in region where the vibration frequency stays close to the structure's eigenfrequency despite changes in wind speed [27]. Abdelkefi et al. (2016) further analyzed how parameters like

Reynolds number and electrical load affect the breadth of the lock-in zone and the harvester's efficiency [28]. These studies demonstrate that VIV-based harvesters are effective but strongly dependent on resonance, which limits performance under variable wind conditions.

Researchers have also investigated alternative geometries and bio-inspired designs to enhance wind energy harvesting. Lee et al. (2019) proposed a leaf-inspired piezoelectric wind harvester that mimics the fluttering of leaves to improve energy conversion efficiency. Their biomimetic device, implemented at MEMS scale, converted wind flow into electrical power and demonstrated the viability of miniaturized piezoelectric harvesters in arrays [29]. Other studies explored transverse galloping phenomena: Abdelkefi et al. (2012) developed an energy harvester using piezoelectric and electromagnetic transducers on a bluff body undergoing galloping oscillations [30]. Galloping-based harvesters leverage aerodynamic instability of non-circular cross-sections (e.g. square cylinders) to produce sustained oscillations over a range of wind speeds [31].

A major challenge in flow-induced vibration harvesters is their typically narrow bandwidth of operation. Efficient energy extraction occurs only near resonance over a limited wind speed range. To broaden this, researchers have proposed nonlinear and multi-modal designs. Masana and Daqaq (2011) studied bistable oscillators and showed that with sufficient excitation, a bistable piezoelectric harvester can exhibit a much wider frequency response than a linear system [32]. Similarly, magnetic coupling has been introduced to achieve multi-stability: Naseer et al. (2019) incorporated magnetic attractors in a VIV piezo harvester to effectively extend the lock-in region and boost power output. Their comparative experiments demonstrated that a harvester with magnetic attachments could sustain large oscillations over a broader range of wind speeds than a linear design [33]. Dai et al. (2016) investigated the orientation of bluff bodies and found that certain cylinder orientations relative to flow can improve energy harvesting efficiency [34]. The influence of mass ratio, damping, and spacing on wake interactions has also been explored for tandem cylinder configurations, indicating that multiple structures can be tuned to enhance or suppress vibrations [35]. These advances in literature underscore the importance of geometry, material nonlinearities, and multi-degree-of-freedom effects in optimizing wind-induced vibration energy harvesters.

Beyond circular cylinders, other shapes and vibration modes have been explored for enhanced or broadband energy harvesting. Galloping oscillations of prismatic bodies (e.g., square or D-shaped cross-sections) have also been used to drive piezoelectric generators. These shapes can exhibit large vibration amplitudes across wind speeds once the critical onset speed is exceeded. Abdelkefi, Hajj and Nayfeh (2012) reported a piezoelectric harvester using transverse galloping of a square bluff body, and derived models for the electromechanical coupling in such flow-induced oscillations [30]. Galloping-based systems often produce lower-frequency, large-amplitude motion which can be advantageous for piezoelectric strains, though they too have an onset threshold and can become non-synchronous at higher speeds.

Recent research has increasingly emphasized integrated computational approaches for energy-harvesting structures. Abdelrheem et al. demonstrated how combining FEM, CFD, and BIM tools can optimize the structural response of pre-stressed wind turbine towers, underscoring the importance of multi-domain numerical methods in capturing fluid–structure interaction behavior [36]. Syed et al. conducted a comparative study on various material and structural configurations for piezoelectric energy harvesting, showing how geometric and material selection directly affects electrical output and mechanical strain distribution—an aspect closely aligned with the objectives of the present study [37]. Additionally, Prasetyo et al. investigated the effect of baffle-plate configurations in gravitational water vortex turbines, illustrating how flow-control elements can significantly modify vortex strength and stability [38]. Although applied in a different context, their findings highlight the broader principle that bluff-body geometry strongly influences downstream wake characteristics, which directly connects to our exploration of cube, cylinder, and sphere configurations.

Building on this prior work, the present research focuses on a bladeless vibration-based wind turbine that converts flow-induced oscillations into electricity via a piezoelectric element. In this study, three different mast tip geometries—a cube, a cylinder, and a sphere—are investigated to identify how bluff body shape influences aerodynamic forcing and energy harvesting performance. While others have studied cylinders extensively, fewer works directly compare

multiple bluff shapes under identical conditions. Numerical simulation and experimental testing are combined to provide a comprehensive evaluation of these designs. CFD is used to determine lift, drag, and axial forces on each prototype, and finite-element modal/harmonic analyses are performed to predict dynamic response and electrical output. These are checked with wind tunnel experiments of physical prototypes with piezoelectric patches. The results will be used to understand how to design the structure geometry and modal properties to obtain the best piezoelectric wind energy harvesting. The procedure, mathematical modelling, simulation and experimental data and general evaluation of the design performance are described below.

METHODOLOGY

A multi-step methodology combining design, simulation, and experimental testing was implemented to evaluate the performance of the bladeless piezoelectric wind turbine with different geometries. The flowchart as shown in Figure 2 outlines the comprehensive research methodology adopted for designing, simulating, and experimentally validating a bladeless vibration-based piezoelectric wind turbine. It integrates conceptual design, computational modeling, and experimental evaluation to assess performance across different bluff body geometries.

The conceptual diagram provided in Figure 3 depicts the basic operation principle of the proposed bladeless vibration-based piezoelectric wind energy harvester. The system comprises of a bluff body placed on the tip of an elastic cantilever rod which is fixed at one end. The flowing air sheds alternating vortices around the sides of the bluff body, which as a result cause transverse vibrations of the structure caused by vortex-induced vibrations (VIV). They are governed by vibrations, resulting in an elastic rod, which is sensitized with a surface mounted piezoelectric sensor at the point of the highest strain energy. The direct piezoelectric effect transforms the mechanical strain on the piezoelectric material into electrical charge and produces a voltage output across the electrodes of the material. The study is anchored on this conceptual set up which offers a small, maintenance free method of harnessing wind energy without rotating blades or lubricated joints that typically require servicing, with an orientation towards simplicity and environmental friendliness. However, long-term durability, fatigue behaviour, and environmental degradation were not evaluated here and remain important areas for future investigation.

Geometric modelling

Three scaled prototype masts were designed, each consisting of a flexible cantilevered rod with a different bluff body at the free end: (1) a cube, (2) a circular cylinder, and (3) a sphere. All three masts shared the same rod dimensions and were made of the same material (a lightweight acrylic sheet) to ensure consistent structural properties. The bluff bodies were sized with comparable characteristic diameters: the cube measured 18 × 18 × 18 mm, the sphere had a diameter of 18 mm, and the cylinder had a diameter of 18 mm

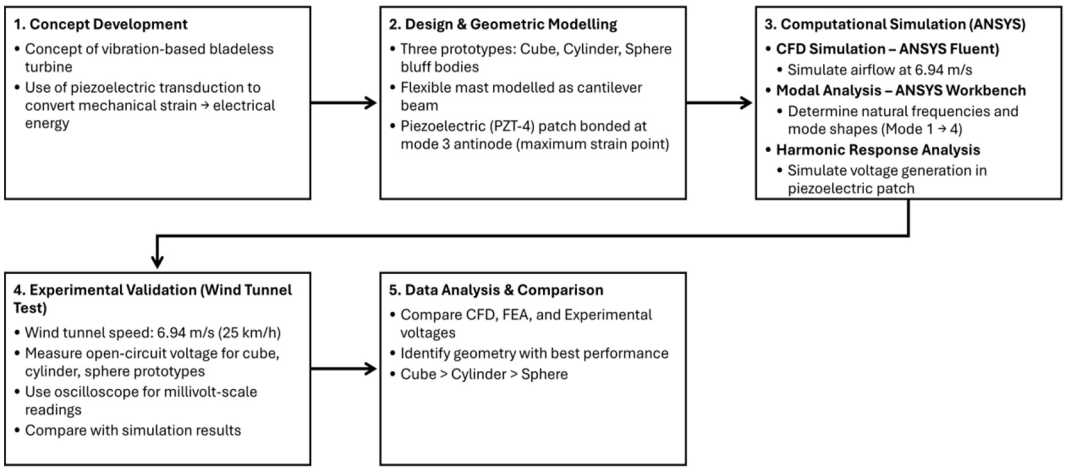

Figure 2. Methodology flowchart illustrating the stepwise process of design, simulation, and experimental validation

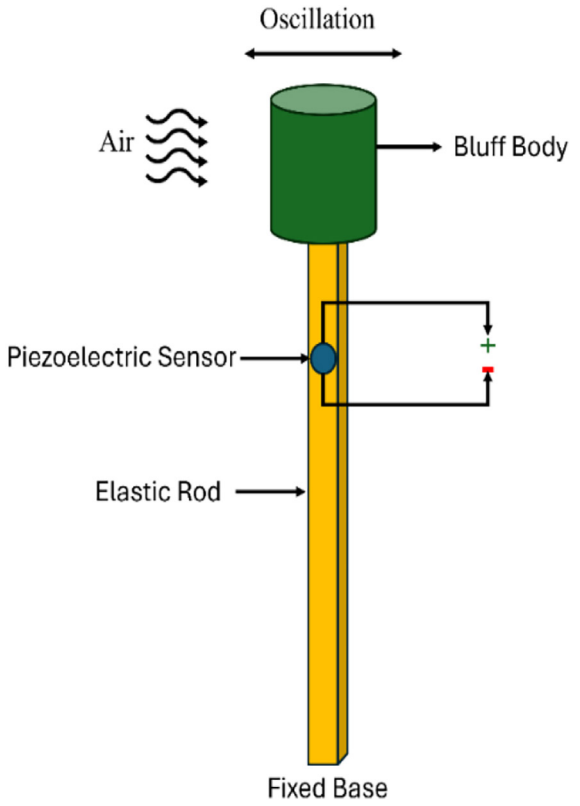

Figure 3. Conceptual diagram of the bladeless piezoelectric wind harvester

with a height of 18 mm. In this configuration, the cube, cylinder, and sphere alter both the effective tip mass and the unsteady aerodynamic forcing, so the observed dynamic response reflects the combined structural–aerodynamic effect of each geometry. The rod material, dimensions, and boundary conditions were kept identical in all cases, ensuring that the bluff body shape (and its associated mass and wake characteristics) is the primary variable, and thus providing a controlled basis for comparing the three prototypes. Figure 4 shows the dimensions of all three prototypes. A thin piezoelectric transducer (PZT-4 type) was surface-bonded near the top of the rod (just below the bluff mass) at the location of maximum deformation identified from the modal analysis (specifically, the antinode of the third bending mode). The PZT-4 transducer polled in the thick direction and wired to an external circuit for voltage measurement. The PZT-4 material used in this study had a density of approximately 7500 kg/m³. Each bluff body was made from acrylic sheet and attached rigidly to the rod tip. The commercially available 3 mm acrylic sheet exhibits a tensile strength of 72 MPa, a flexural strength of about 112 MPa, and a Young's modulus of nearly 3.2 GPa. These properties make it a strong yet lightweight material suitable for structural and experimental applications. The base of the rod was clamped to mimic a cantilever boundary condition. Three-dimensional models of each prototype were created in ANSYS Design Modeler as shown in Figure 5, and a surrounding computational fluid domain was constructed to simulate wind tunnel flow conditions.

Computational fluid dynamics (CFD)

CFD simulations were performed in ANSYS Fluent to analyze the airflow around each prototype and compute aerodynamic force coefficients. Each geometry (cube, cylinder, sphere on rod) was placed in a virtual wind tunnel domain with defined inlet, outlet, and wall boundary conditions. For each case, the steady-state solver was employed to converge the flow field. The drag (F_D), lift (F_L), and axial (F_A) forces were recorded via ANSYS reports for each geometry.

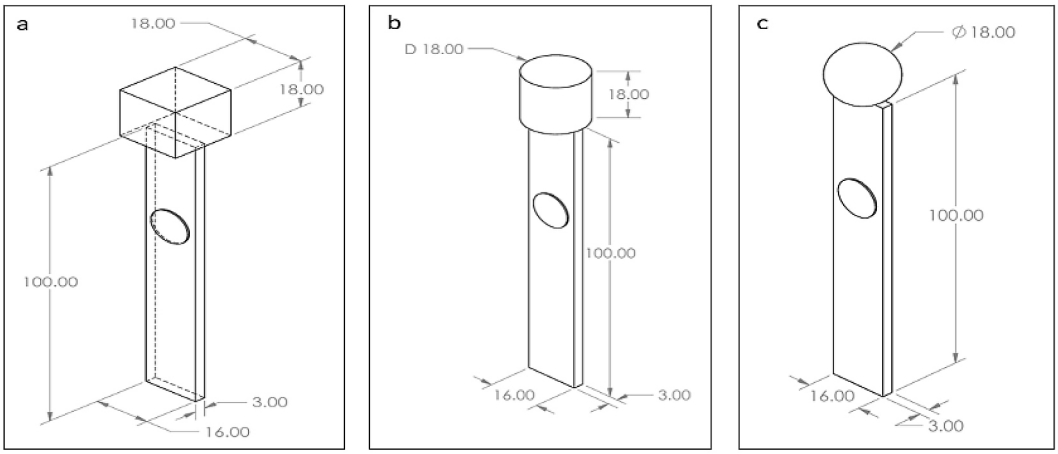

Figure 4. Dimensions of prototypes when bluff body is: (a) cube, (b) cylinder, (c) sphere

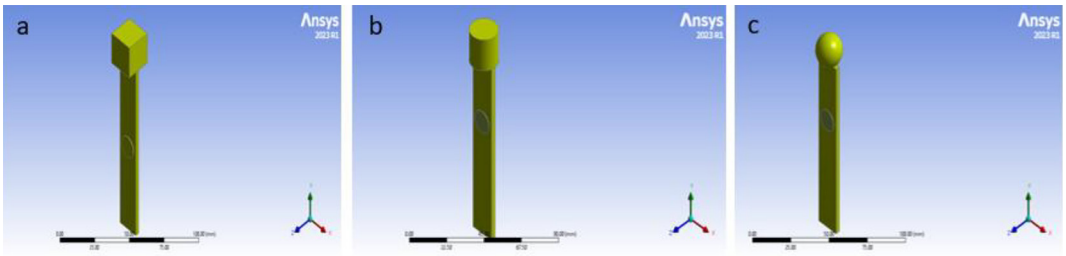

Figure 5. 3D Models of Prototypes when bluff body is: (a) cube, (b) cylinder, (c) sphere

The computational fluid domain was constructed, as shown in Figure 7, following standard wind tunnel simulation guidelines to minimize boundary effects and ensure realistic flow development [39–41]. To ensure the airflow behavior around the model was accurate, the computational domain was configured to the specific dimensions. The domain was configured such that the entrance region was extended to four times the bluff body's characteristic length. This configuration allows the airflow to develop before reaching the turbine. A downstream region of the domain to eight times the characteristic length allows the computational domain to capture the wake, flow streamlines, and velocity. The sides of the domain include a clearance of four times the characteristic length to mitigate wall effects and flow interference.

All cases utilized a Hex-Dominant volume mesh with local refinement around the mast and bluff body to accurately capture the shear layers and the near wake. This approach resulted in a predominately hexahedral core with transitional Tet/Pyr/Wedge cells around areas of complex curvature and the boundary-layer growth region. The computational domain employed named boundary features of inlet, outlet, symmetry, and wall (mast and bluff body). The meshing approach taken for cube, cylinder, and sphere shapes geometries provided both numerical accuracy and computational sufficiency for the subsequent CFD simulations. Each of the three cases was assigned a consistent global element size of 5 mm. To accurately capture the boundary-layer effects and flow separation phenomena, a refined near-wall mesh of 0.025 mm was implemented. Table 1 highlights the meshing characteristics. The orthogonal quality remained above the minimum acceptable limit of 0.85, with the cube prototype attaining a peak quality of 0.9435, followed by the cylindrical prototype at 0.9372, and the sphere prototype with a quality of 0.8838, thus within acceptable bounds. As a result of well-structured mesh with skewness and distortion within an acceptable range, stable convergence was achieved, leading to dependable outcomes in the prediction of aerodynamic forces and the assessment of flow fields. Figures 6, 7 and 8 show the meshing of the three models with the mast configured as a cube, cylinder, and sphere, respectively.

All three bluff-body configurations (cube, cylinder, and sphere) were analyzed in ANSYS Fluent under the same boundary conditions. A pressure-based RANS solver with the Standard k–ε turbulence model and standard wall functions was employed. Given the geometric simplicity of the bluff bodies and the focus on comparative aerodynamic trends rather than detailed transient vortex dynamics, the *k–ε* model offered an appropriate balance between accuracy and computational cost. The computational domain was defined with a uniform inlet velocity of 6.944 $m \cdot s^{-1}$ (25 $km \cdot h^{-1}$), a zero-gauge pressure outlet, and symmetry boundaries on the remaining far-field planes; the mast and bluff-body surfaces were treated as no-slip walls. Symmetry boundary conditions were applied on the lateral surfaces to approximate free-stream conditions. Because the computational domain was extended to four times the bluff body diameter on each side, the wake and shear layers did not interact with the side boundaries, making symmetry a valid approximation for

Table 1. Meshing characteristics

Case	Element size (global)	Near wall Mesh element size	Nodes	Elements	Orthogonal quality
Cube	5 mm	0.025 mm	162,602	162,106	0.9435
Cylinder	5 mm	0.025 mm	164,793	164,676	0.9372
Sphere	5 mm	0.025 mm	160,491	168,655	0.8838

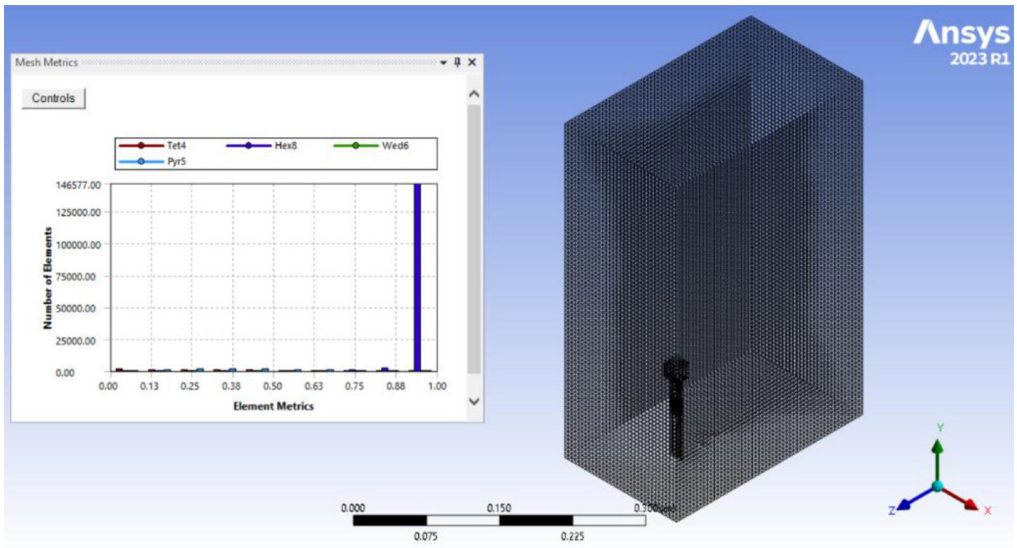

Figure 6. Mesh generation of the computational domain with cube-shaped bluff body

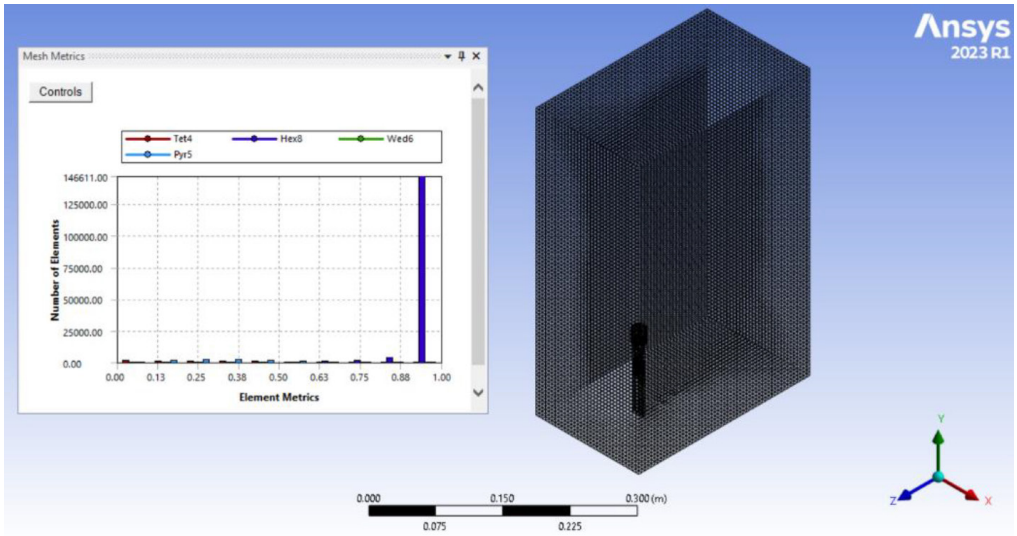

Figure 7. Mesh generation of the computational domain with cylinder-shaped bluff body

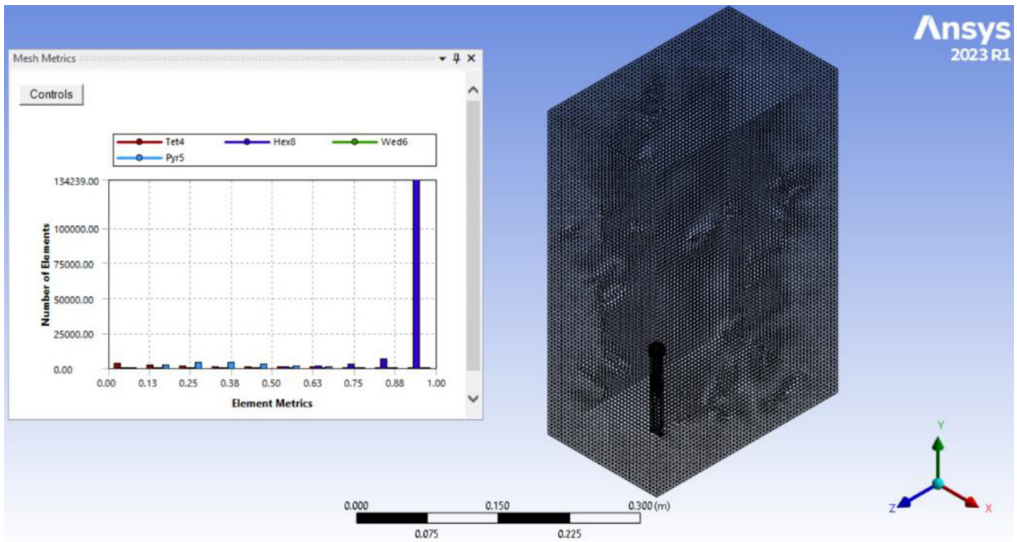

Figure 8. Mesh generation of the computational domain with sphere-shaped bluff body

an isolated body. The bluff body was used as the characteristic dimension for the Reynolds number because it is the primary source of flow separation, vortex shedding, and unsteady aerodynamic forcing in the system. To determine whether the flow was laminar or turbulent, the Reynolds number was calculated as follows:

$$Reynolds\ No. = R_e = \frac{\rho V D}{\mu}$$
$$R_e = \frac{1.225 \times 6.9444 \times 0.018}{1.8 \times 10^{-5}} \quad (1)$$
$$R_e = 8506\ (Turbulent\ Flow)$$

Transition to turbulent wake flow in bluff bodies occurs at relatively low Reynolds numbers because the separated shear layers become unstable soon after detachment. For circular cylinders, experimental and numerical studies consistently show that turbulent vortex shedding develops for $R_e \geq 2 \times 10^3$ [42–44], as the separated shear layers transition rapidly to turbulence. Since operating Reynolds numbers were 8506, the flow lies well within the turbulent regime where turbulent vortex shedding dominates, supporting the use of a turbulence model. Table 2 summarizes the CFD boundary conditions applied in ANSYS, including inlet velocity, outlet pressure, wall constraints, and fluid properties. Figure 9 illustrates the boundary condition setup, showing velocity inlet, pressure outlet, symmetry planes, and no-slip wall regions.

Modal analysis

A modal analysis of the mast (rod plus attached mass) was conducted in ANSYS Workbench to determine its natural frequencies and mode shapes. A 3D finite-element model of the structure was created, with the rod meshed using hexahedral elements and the tip mass as a rigid body. The same material properties (elastic modulus and density) from the CFD analysis were used in the modal analysis. In the modal analysis, the piezoelectric transducer was included as part of the structural model so that its mass and stiffness contributions were properly considered. However, the electromechanical coupling was not activated

Table 2. Boundary conditions

Item	Setting
Inlet	Velocity inlet, 6.9444 m/s
Outlet	Pressure outlet, 0 Pa gauge
Side/Top/Bottom	Symmetry (slip)
Walls	No-slip (mast + bluff body)
Turbulence model	Standard k-ε, standard wall function
Convergence criteria	1e-05
Temperature	300 K
Solver	Steady (3D)
Density of air	1.225 kg/m^3
Viscosity of air	1.8×10^{-5} Pa-s

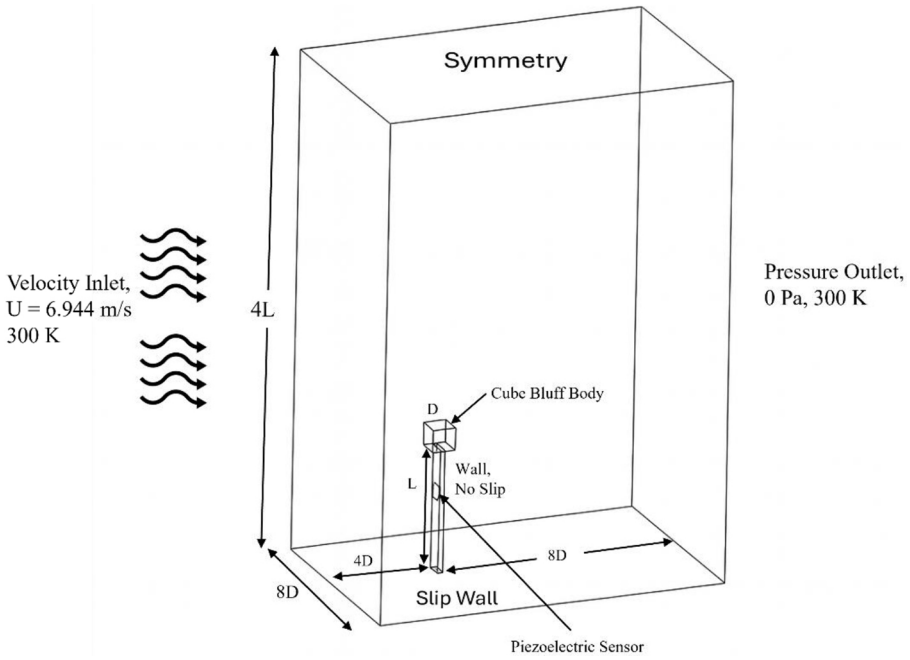

Figure 9. Computational domain and boundary conditions for the CFD simulation

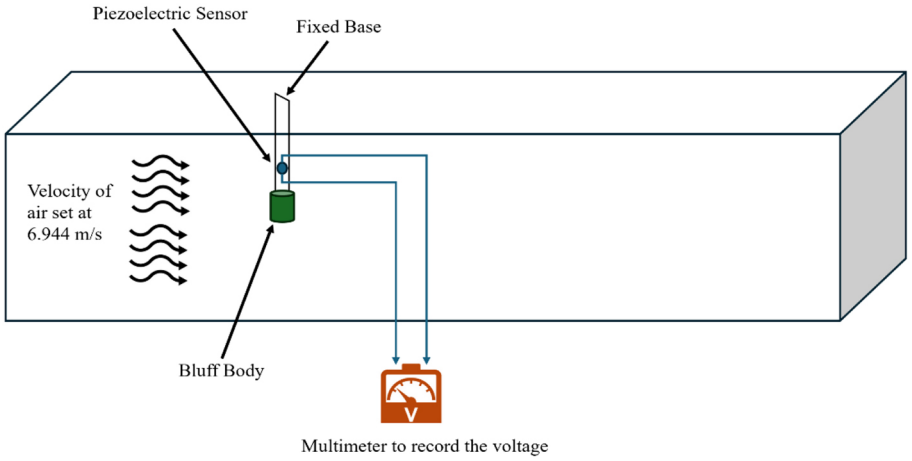

Figure 10. Schematic representation of the wind tunnel experimental setup for piezoelectric wind turbine testing

during this step because the purpose of the modal analysis was solely to determine the natural frequencies and mode shapes of the mast–bluff body system. At this stage, the transducer functions purely as a passive structural layer rather than an active piezoelectric component. The boundary condition at the base was fixed. The analysis extracted the first several modes for all prototypes.

Harmonic analysis

An electromechanical harmonic analysis was performed using ANSYS to compute the voltage output of the piezoelectric transducer. The modal analysis results (natural frequencies and mode shapes) were used for this step. An equivalent aerodynamic force is applied to the mast, sweeping through a range of frequencies around the expected vortex shedding frequency and higher modes. The piezoelectric transducer was modelled with the full piezoelectric constitutive matrices (using PZT-4 properties as defined in the ANSYS engineering data). For each natural mode, the steady-state structural response and the resulting open-circuit voltage across the transducer electrodes were computed. From this, the peak voltage output was identified, which typically occurred near the fundamental bending resonance. Nonlinear multi-modal coupling effects are not explicitly modelled here and are identified as an avenue for future work.

Experimental testing

Experiment was carried out in a controlled wind tunnel to measure the actual performance of each prototype. The experiments used a low-speed wind tunnel with a test section large enough to avoid significant blockage effects. Each mast prototype (cube, cylinder, sphere-tipped prototype) was mounted one at a time in the test section with the base clamped rigidly. The experiment is performed at a wind speed of 6.944 m/s. At this speed, the corresponding Reynolds number based on bluff body diameter was on the order of 10^4. The oscillations of the mast were noted, and the induced voltage in the piezoelectric transducer was recorded by a multimeter. For the bladeless piezoelectric wind turbine, the wind tunnel schematic and experimental setup are shown in Figure 10.

Mathematical modelling

Structural dynamics

In this section, the mast with tip mass is represented by an equivalent SDOF oscillator in modal coordinates, which corresponds to a single bending mode of the cantilever. This lumped model is used only to provide a compact description of the mass–stiffness–damping balance and to interpret resonance behaviour. A lumped-parameter model is given by:

$$m_{eq}\ddot{y}(t) + c_{eq}\dot{y}(t) + k_{eq}y(t) = F_{lift}(t) \quad (2)$$

where: $y(t)$ is the transverse displacement (in the direction of wind force), m_{eq} is the modal mass (which includes the rod's distributed mass and the tip mass contribution), c_{eq} is the damping (from structural and aerodynamic sources), and k_{eq} is the effective stiffness of the mast. The natural frequency is:

$$f_n = \frac{1}{2\pi}\sqrt{\frac{k_{eq}}{m_{eq}}} \quad (3)$$

where: k_{eq} is equivalent stiffness of the system (N/m), m_{eq} is equivalent mass of the system (kg). For a cantilever beam of length L with a tip mass M, an approximate formula for the first bending frequency is:

$$f_1 = \frac{1.875^2}{2\pi L^2}\left(\sqrt{\frac{EI}{mL + 0.242ML}}\right) \tag{4}$$

where: EI is the flexural rigidity of the rod and m the mass per length of the rod.

The 1.875 factor is the first-mode eigenvalue for a uniform cantilever without tip mass [45], and the 0.242 M term is an approximation for the tip mass effect (increasing the modal mass). Higher modes have eigenvalues 4.694 (second bending) and 7.855 (third bending) for a bare cantilever [45], but the heavy tip mass lowers these frequencies significantly and also alters mode shapes. The exact eigenvalue problem was solved via FEA modal analysis rather than using closed-form approximations. The modal damping ratio ζ for the fundamental mode was small, estimated at about 1% from free decay in still air. Aerodynamic damping in cross-flow VIV can be negative (excitative) near lock-in, effectively absorbed into the forcing term $F(t)$ in the above equation.

Piezoelectric coupling and voltage generation

The geometric model of the bladeless piezoelectric wind turbine consists of a bluff body mounted on a flexible mast, with a piezoelectric transducer attached near the region of maximum strain. The bluff body interacts with the air entering to provide the mast with vortex-induced vibrations. The vibrations cause deformation in the bonded piezoelectric element resulting in electrical voltage generation using the direct piezoelectric effect. The simplified schematic as demonstrated in Figure 11, depicts the aerodynamic interaction process, structural deformation and resultant process of electromechanical energy conversion. When the mast oscillates, the bonded piezoelectric transducer experiences cyclic strain. Under open-circuit conditions, a charge accumulates on the electrodes, resulting in a voltage. The piezoelectric constitutive equations (in strain-charge form) are:

$$S_{ij} = s^E_{ijkl}T_{kl} + d_{kij}E_k \tag{5}$$

$$D_i = d_{ikl}T_{kl} + \epsilon^T_{ik}E_k \tag{6}$$

where: S_{ij} is strain, T_{kl} stress, E_k electric field, D_i electric displacement, s^E_{ijkl} compliance (elastic flexibility) at constant electric field, d_{kij} the piezoelectric strain coefficients, and ϵ^T_{ik} the permittivity (dielectric constant at constant stress) [45].

For a unimorph cantilever transducer in the 31 mode (piezo transducer oriented such that it is strained axially (1-direction) by bending along the beam length, generating an electric field in thickness (3-direction)), a simplified one-dimensional model can be used. The bending of the beam causes a longitudinal strain $\in_{xx}$ in the piezo layer. The open-circuit voltage V can be related to the strain by:

$$V = -\left(\frac{d_{31}Y_p t_p}{\varepsilon^T_{33}}\right)\epsilon_{xx} \tag{7}$$

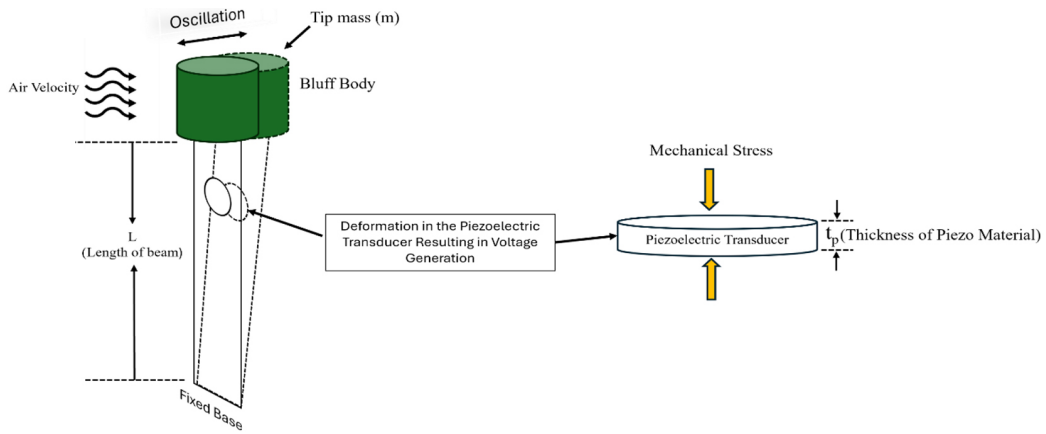

Figure 11. Schematic representation of the geometric model showing voltage generation through piezoelectric transducer

to first order [45]. Here, d_{31} is the piezoelectric constant (~–5.2 × 10^{-10} m/V for PZT-4), Y_p the Young's modulus of the piezo (~6.3 × 10^{10} Pa for PZT-4), t_p the thickness of the piezo layer (our patch ~0.5 mm), ε_{33}^T the permittivity in the thickness direction ($\varepsilon_{33}^T \approx 5.6 \times 10^{-9}$ F/m for PZT-4), and $\in_{xx}$ is the effective average strain in the patch. The piezoelectric voltage generation mechanism in this study is based on the d_{31} effect, where mechanical stress in the x-direction causes electric displacement in the z-direction. The total charge Q generated on the piezoelectric electrodes due to this effect is given by:

$$Q = \int_A D_3 dA \tag{8}$$

where: D_3 is the electric displacement in the z-direction, A is the electrode area.

The electric displacement D_3 is related to the stress T_{xx} through the piezoelectric constant d_{31} as:

$$D_3 = d_{31} T_{xx} \tag{9}$$

Substituting this into the Equation 8:

$$Q = d_{31} \int_A T_{xx} dA \tag{10}$$

The voltage generated across the piezoelectric transducer is given by:

$$V = \frac{Q}{C} \tag{11}$$

where: C is the capacitance of the piezoelectric transducer.

$$C = \frac{\varepsilon_{33}^T A}{t_p} \tag{12}$$

Combining the above equations:

$$V = \frac{\left(d_{31} \int_A T_{xx} dA\right)}{\frac{\varepsilon_{33}^T A}{t_p}} = \frac{d_{31} t_p}{\varepsilon_{33}^T A} \int_A T_{xx} dA \tag{13}$$

Assuming uniform stress over the transducer, and using Hook's Law,

$$T_{xx} = Y_p \epsilon_{xx} \tag{14}$$

Substituting in Equation 13,

$$V = \frac{d_{31} t_p}{\varepsilon_{33}^T A} \int_A Y_p \epsilon_{xx} dA \tag{15}$$

Where $\in_{xx}$ is uniform over the area (valid assumption for thin or small patches located in high-curvature regions):

$$V = \left(\frac{d_{31} Y_p t_p}{\varepsilon_{33}^T \times A}\right) \epsilon_{xx} \times A = \left(\frac{d_{31} Y_p t_p}{\varepsilon_{33}^T}\right) \epsilon_{xx} \tag{16}$$

In our design, the transducer is located where the bending curvature (hence strain) is largest. The strain $\in_{xx}$ is proportional to the beam curvature $\kappa(x)$ at that location:

$$\epsilon_{xx} = \kappa(x) \times y_p \tag{17}$$

where: γ_p is the distance from the neutral axis to the piezo layer.

Thus, voltage is ultimately proportional to bending curvature (and thus proportional to deflection for small vibrations). The finite-element harmonic analysis directly computes this via the coupled-field elements, but the above relation provides a useful approximation. In summary, the mathematical model ties together the fluid dynamics, the structural dynamics, and the electromechanical coupling (voltage ~ strain). This provides a framework to interpret the results that follow.

RESULTS

The cube-shaped bluff body prototype exhibits the classic footprint of a sharp-edged bluff body. Velocity contours show immediate fixed separation at the leading edges and the formation of strong corner vortices, with little reattachment on the lee faces. The separated shear layers are relatively thick and undergo three-dimensional roll-up, feeding a broad, high-deficit recirculation zone that persists several cube widths downstream before recovering. The alternating wake structures are evident but less phase-coherent than in the circular case, which manifests in the frequency domain as a broadened peak in the lift spectrum with appreciable sideband content. Aerodynamically, the cube produces the highest time-averaged drag and substantial fluctuating lift of the three geometries. However, the reduced spectral purity means it provides strong excitation potential but a less "clean" lock-in compared to a cylinder. Figure 12 presents the velocity contours around the cube-shaped bluff body from side and top views, highlighting wake formation and flow separation.

For the cylinder-shaped bluff body prototype, the velocity contours reveal a stagnation region at the nose, forming two comparatively thin, symmetric shear layers. Figure 13 depicts

the velocity contours around the cylinder-shaped bluff body from side and top views, showing symmetrical wake.

The sphere-shaped bluff body shows the most streamlined behavior. Contours indicate a strong stagnation at the forward pole, followed by later separation than for the cylinder, yielding a shorter recirculation region and smoother shear layers. The wake was the narrowest of the three and exhibits the fastest velocity recovery. Figures 14 show the velocity contours around the sphere-shaped bluff body from side and top views.

Table 3 compares the steady aerodynamic force components obtained from CFD for the three geometries at a wind speed of 6.94 m/s. All prototypes experienced a dominant drag force in the flow direction and much smaller lift and axial forces (axial meaning along the mast axis, here vertical). The sphere-topped mast had the lowest drag (about 0.084 N), as expected given the sphere's streamlined shape and lower drag coefficient. The cube, with its bluff profile, produced the highest drag (~0.090 N), roughly 7% higher than the sphere. The cylinder was intermediate (~0.085 N). The lift forces were an order of magnitude smaller than drag for all shapes. For the sphere, ANSYS force reports gave mean drag of ≈ 0.08422 *N*, mean lift ≈ 0.00403 *N*, and axial force of ≈ 3.70×10^{-4} *N* at 6.9444 m s^{-1}. The cube generally registers the highest mean drag due to its sharp-edged separation and a sizeable unsteady lift, yet with a broader spectral peak than the cylinder, indicating less regular shedding. At the tested wind speed of 6.94 m/s, the cube generates the strongest aerodynamic forcing due to its sharp-edged separation and high drag, making it the most effective exciter of the mast. The cylinder produces slightly lower forcing but exhibits more coherent vortex shedding, resulting in a moderate yet stable excitation response. The sphere, with its streamlined flow and weak separation, provides the lowest excitation amplitude. It should be noted that this ranking (cube > cylinder > sphere) reflects the behavior at the tested Reynolds number; changes in wind speed can modify vortex-shedding coherence

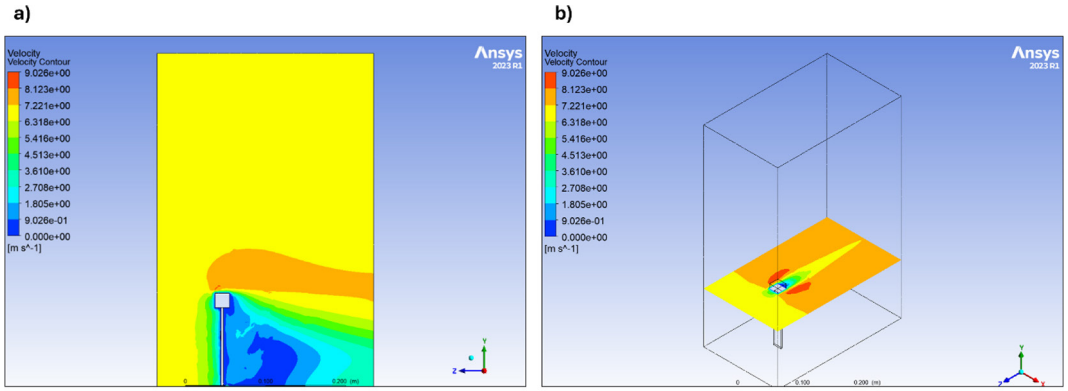

Figure 12. Velocity contour around the cube-shaped bluff body: (a) side view, (b) top view

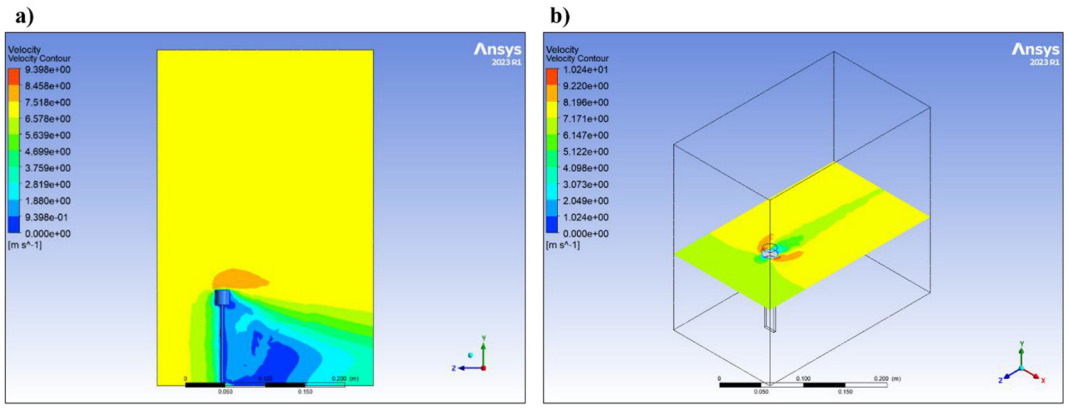

Figure 13. Velocity contour around the cylindrical-shaped bluff body: (a) side view, (b) top view

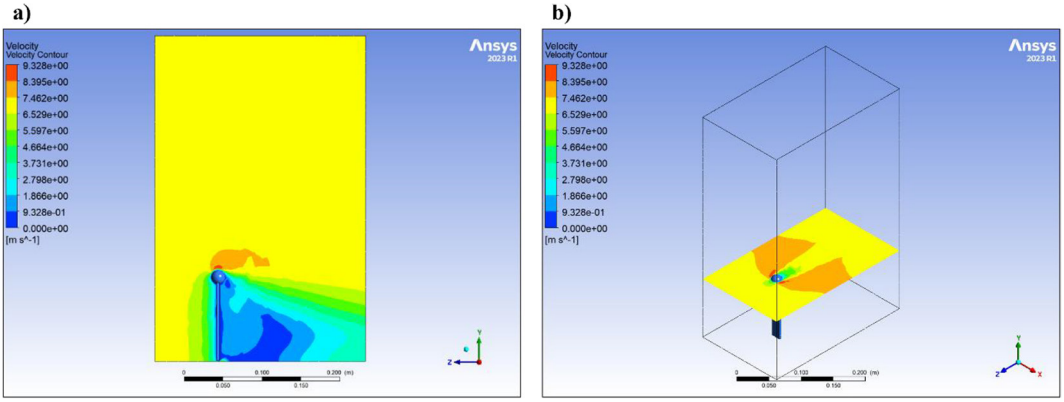

Figure 14. Velocity contour around the sphere-shaped bluff body: (a) side view, b) top view

and frequency alignment, and thus the relative excitation efficiency of the bluff bodies may vary under different flow conditions.

Modal analysis and frequencies

The findings of the modal analysis performed with ANSYS offer valuable information on the dynamic behavior of the three prototypes with different bluff body geometries (cube, cylinder, and sphere). Of note, the modal frequencies in the first four modes are most helpful in characterizing the wind-related dynamic response of the structures (i.e. wind-induced dynamic vibrations). In Mode 1, the sphere prototype had the highest natural frequency (~ 85 Hz), followed by the cube (~ 75 Hz), and then the cylinder (~ 70 Hz). This suggests that the mast configuration with a sphere was structurally stiffer, and was able to better resist low frequency vibrations. This is likely due to the sphere's geometry which is symmetrical and streamlined. On the other hand, the cylinder is more symmetrical compared to the other shapes, but in the first mode, it has lower stiffness and/or different mass distribution allowing it to offer slightly less resistance. The same pattern is observed in Mode 2, where the sphere again has the highest frequency at 447 Hz, which is significantly greater than the cube's 350 Hz and the cylinder's 370 Hz. The higher frequency observed in the sphere suggests that higher-order bending modes are more pronounced in less bluff geometries, likely due to lower drag-induced displacements.

Mode 3 also exhibits a curvature pattern that produces strong bending gradients at the piezoelectric location, causing the PZT layer to undergo larger alternating tensile–compressive strains per vibration cycle than in the lower or higher modes. The combined effects of closer frequency alignment with the vortex-shedding excitation and higher modal curvature result in significantly higher strain energy being transferred to the piezoelectric material, which explains the pronounced voltage amplification observed at this mode. In this study, Mode 3 was the most important mode because, at the tested wind speed of 6.94 m/s, highest model curvature is produced along the rod span, resulting in the highest modal strain and electrical output. This dominance of Mode 3 is specific to the tested Reynolds number; however, at different wind speeds, the shedding frequency and frequency alignment may shift, potentially altering which mode is most strongly excited. For the sphere, Mode 3 occurs at 700 Hz, which is higher than the cylinder (~ 640 Hz) and the cube (~ 620 Hz). This is significant in regard to piezoelectric energy harvesting because the piezoelectric transducer responds strongly to strain, and Mode 3 exerts more strain on the mast than the other modes. In Mode 4, all prototypes exhibit

Table 3. Aerodynamic force comparison (CFD results at 6.94 m/s)

Bluff body geometry	Drag force F_D (N)	Lift force F_L (N)	Axial force F_A (N)
Cube	0.090 N	0.005 N	0.0004 N
Cylinder	0.085 N	0.004 N	0.00037 N
Sphere	0.084 N	0.004 N	0.00037 N

significantly higher frequencies. Again, the sphere led with 1161 *Hz* reflecting its structural rigidity. The cylinder followed with 912 *Hz*, while the cube registered ~900 *Hz*. These high-frequency modes are typically less relevant for energy harvesting unless extremely high wind speeds are present. However, they still indicate the robustness of each structure under extreme dynamic loading. Table 4 presents the natural frequencies for all cases.

The mode shapes indicated that the maximum curvature for Mode 1 was at the tip, while for Mode 3 it peaked along the span of the mast. In our design, placing the piezo transducer at the Mode 3 antinode (where deformation is high) was intended to capture significant strain energy from mode contributions. Tables 5, 6, and 7 show the different mode shapes for the bluff bodies configured as a cube, cylinder, and sphere, respectively.

Piezoelectric voltage output

The most important performance indicator was the electrical output from the piezoelectric transducer. Simulations were conducted using the aerodynamic forces derived from the CFD analysis. The harmonic response analysis in ANSYS showed that various bluff body geometries affected the voltage produced by the piezoelectric transducer. The voltage values in Table 8 were taken from the harmonic response analysis conducted in ANSYS concerning different bluff body geometries. The electrical output from the piezoelectric transducer was estimated for every mode under aerodynamic loading. Modes 1 and 2 recorded relatively lower voltages for all prototypes, while Mode 3 produced the highest output, confirming it as the most effective for energy harvesting. Although Mode 4 showed a decline in output relative to Mode 3, it was still higher than Modes 1 and 2. The drop in voltage after Mode 3

Table 4. Mast natural frequencies (ANSYS modal analysis)

Prototype	Mode 1 (Hz)	Mode 2 (Hz)	Mode 3 (Hz)	Mode 4 (Hz)
Cube	~75	~350	~620	~900
Cylinder	~70	~370	~640	~912
Sphere	~85	~447	~700	~1161

Table 5. Mode shapes of the prototype with cube-shaped bluff body

Mode shapes of the prototype with cube-shaped bluff body	
Mode 1	Mode 2
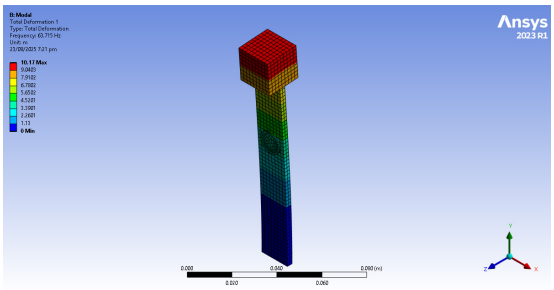	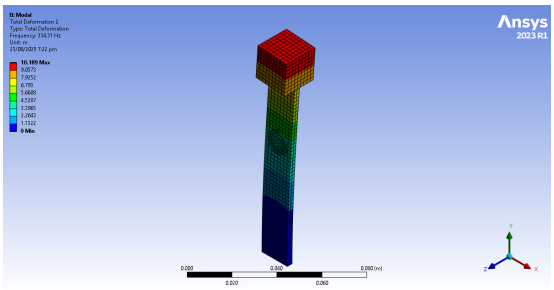
Mode 1 when bluff body is cube	*Mode 2 when bluff body is cube*
Mode 3	Mode 4
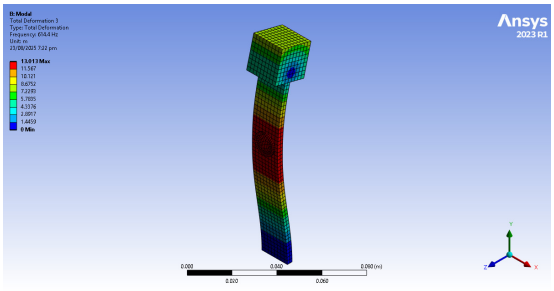	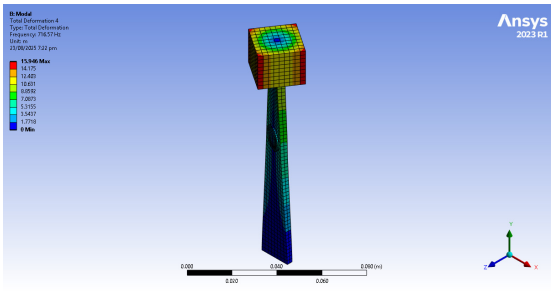
Mode 3 when bluff body is cube	*Mode 4 when bluff body is cube*

Table 6. Mode shapes of the prototype with cylindrical-shaped bluff body

Mode shapes of the prototype with cylindrical-shaped bluff body	
Mode 1	Mode 2
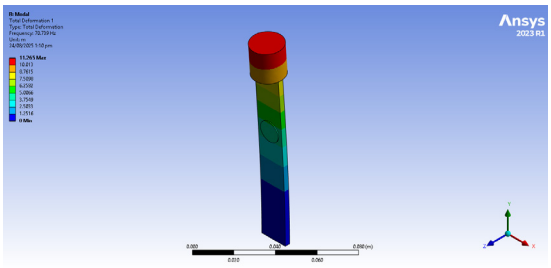	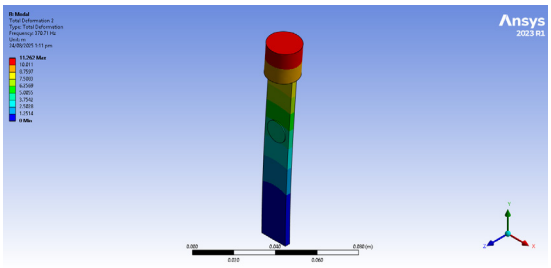
Mode 1 when bluff body is cylinder	*Mode 2 when bluff body is cylinder*
Mode 3	Mode 4
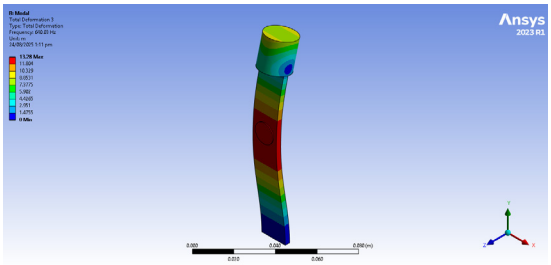	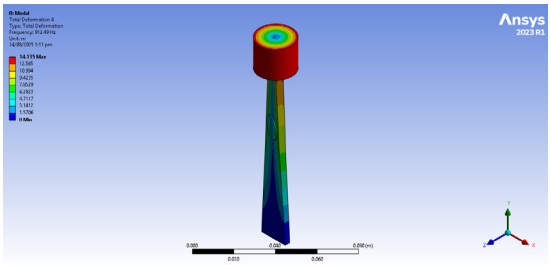
Mode 3 when bluff body is cylinder	*Mode 4 when bluff body is cylinder*

Table 7. Mode shapes of the prototype with sphere-shaped bluff body

Mode shapes of the prototype with sphere-shaped bluff body	
Mode 1	Mode 2
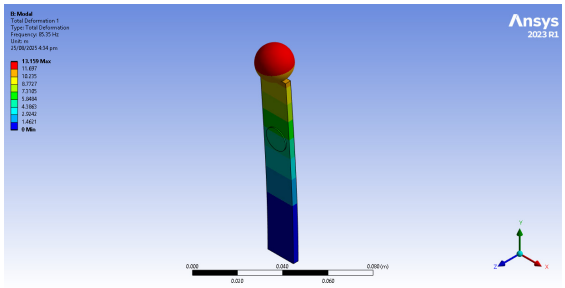	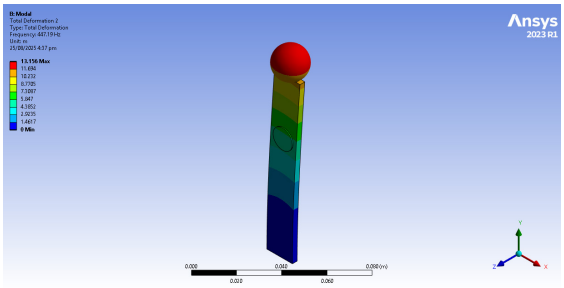
Mode 1 when bluff body is sphere	*Mode 2 when bluff body is sphere*
Mode 3	Mode 4
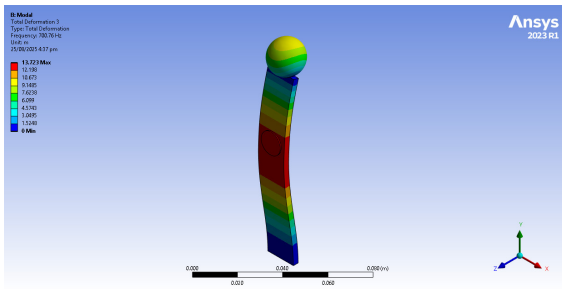	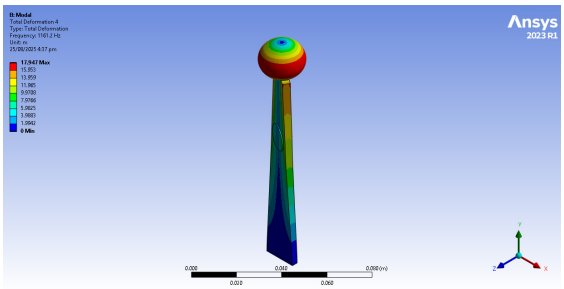
Mode 3 when bluff body is sphere	*Mode 4 when bluff body is sphere*

is primarily related to the deformation pattern of the higher modes. A piezoelectric patch generates voltage only when it undergoes mechanical strain, and the strain distribution along the rod depends on the curvature shape of each mode. While Mode 3 produces strong bending at the patch location, the higher modes exhibit much smaller curvature and deformation in that region. As a result, the

Table 8. Voltage values at different modes

Mode	Cube (mV)	Cylinder (mV)	Sphere (mV)
Mode 1	2.505	1.914	1.288
Mode 2	2.906	2.088	1.771
Mode 3	5.145	4.1813	3.227
Mode 4	4.008	2.958	2.415

piezoelectric layer experiences significantly less strain, and the voltage output naturally decreases. This geometric reduction in strain dominates the response, even before considering additional factors such as reduced aerodynamic forcing or higher structural damping at elevated frequencies. These observations are supported by Figure 18, which depicts the voltage trends for all four modes.

Among the different types of masts, the cube-tipped mast produced the greatest voltage output (~ 0.005145 Volts), the cylinder-tipped mast was in the second position (~ 0.00418 Volts), and the sphere-tipped mast produced the least output (~ 0.00322 Volts) as shown in Figure 15, 16 and 17 respectively. Such results correlate well with the dynamics of wakes produced and the spatial flow separation associated with each form. Cubes produced strong, unsteady aerodynamic vortex and aerodynamically supersensitive mast port deflections. This results in large piezoelectric transducer

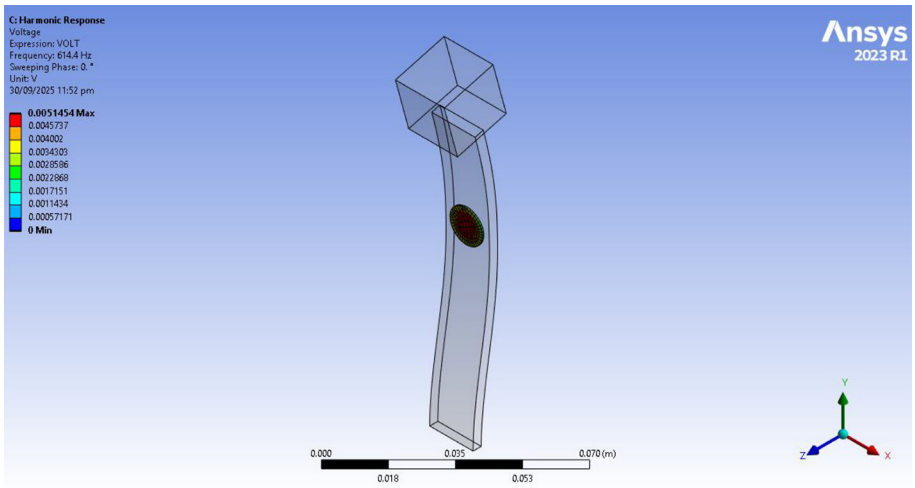

Figure 15. Simulated voltage output with cube bluff body

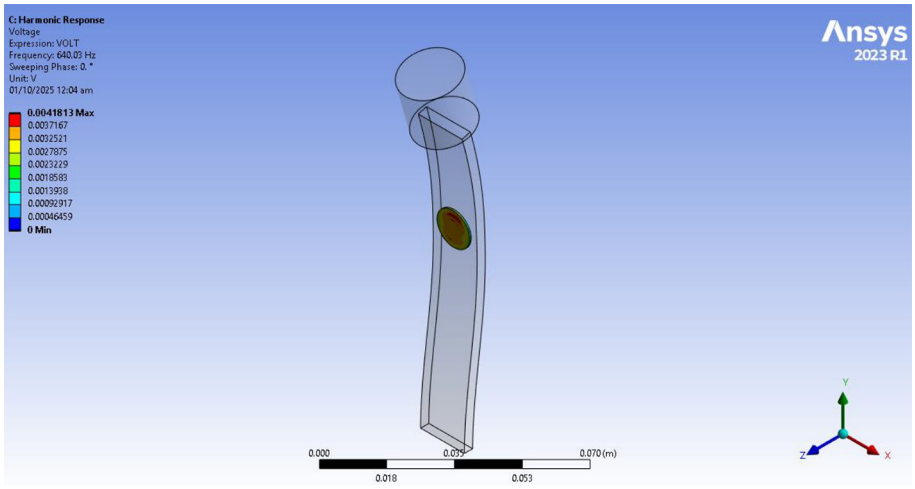

Figure 16. Simulated voltage output with cylindrical bluff body

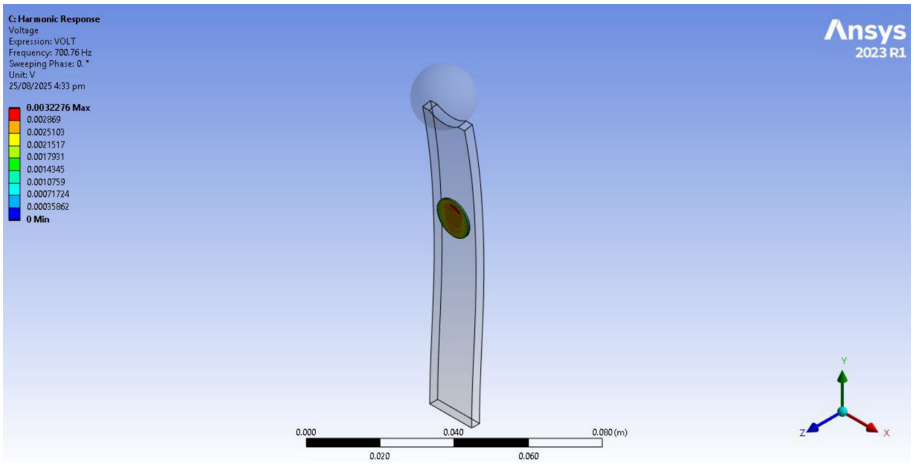

Figure 17. Simulated voltage output with sphere bluff body

strains. As the cylinder was more aerodynamically refined, the flow oscillation patterns changed to more stable and symmetrical, and thus, moderate. The strongest flow of the sphere was associated with the smoothest wake, thus flow unsteadiness was at a minimum, which explains the small strains and low voltage output results.

Experimental results

The experiment was conducted in a closed-circuit subsonic wind tunnel available in the laboratory. The free-stream velocity was maintained at 25 km/h (6.944 m/s) for all tests to ensure comparability with the numerical simulations. Three bluff body prototypes were fabricated with identical characteristic dimensions. To ensure uniformity, the masts were manufactured from the same structural material and had identical lengths and cross-sections across all cases. This ensured that any differences in electrical output could be attributed directly to prototype geometry rather than mast properties. A commercial piezoelectric transducer was bonded to the mast at the location of maximum strain energy as identified from the third mode shape in the modal analysis. Figure 19 shows the prototypes with cube, cylinder, and sphere bluff body geometries attached to piezoelectric transducers. The open-circuit voltage across the PZT transducer was recorded using a high-sensitivity oscilloscope with millivolt resolution. The wind tunnel tests for each prototype were conducted under steady-state flow conditions, with data acquisition spanning 60–90 seconds for each

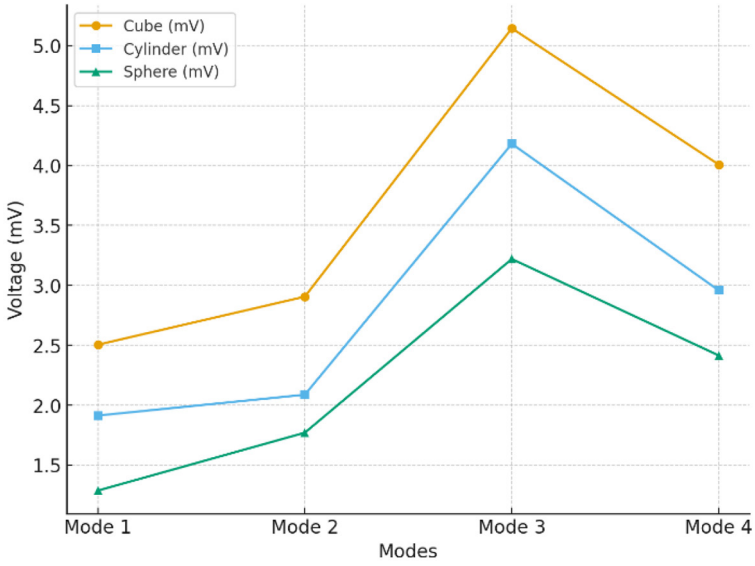

Figure 18. Voltages produce at different modes for different prototypes

Figure 19. Prototypes

run. Multiple runs were performed per prototype to establish repeatability and to capture the inherent variability in flow-induced vibrations.

Figure 20a presents the experimental setup with the cube-shaped bluff body, Figure 16 (b) shows the setup with a cylindrical-shaped bluff body, and Figure 16c illustrates the setup with a spherical-shaped bluff body.

The shape of the prototype had a direct impact on measuring the output voltage. The cube-shaped prototype produced a maximum output of 5 mV with a satisfactory steady amplitude during several measurements. The cylinder prototype produced a slightly lower output of 4 mV. The weakest prototype was the sphere with a maximum voltage output of 3 mV, the smooth surface of the sphere created an early, though symmetrically, flow-separation.

The cube, cylinder and sphere prototype shapes in the comparative analysis produced a clear and consistent order of performance: cube, cylinder, sphere. The cube was most effective at harvesting energy, with high voltage output, due to its high drag configuration, while the cylinder was of balanced design. The sphere was the least effective, having smooth aerodynamics which caused flow suppression. The relative performance trends of the three prototypes (cube > cylinder > sphere) were consistent between the experimental and numerical results, although the absolute voltage values for the sphere showed a noticeable discrepancy. This is likely because the

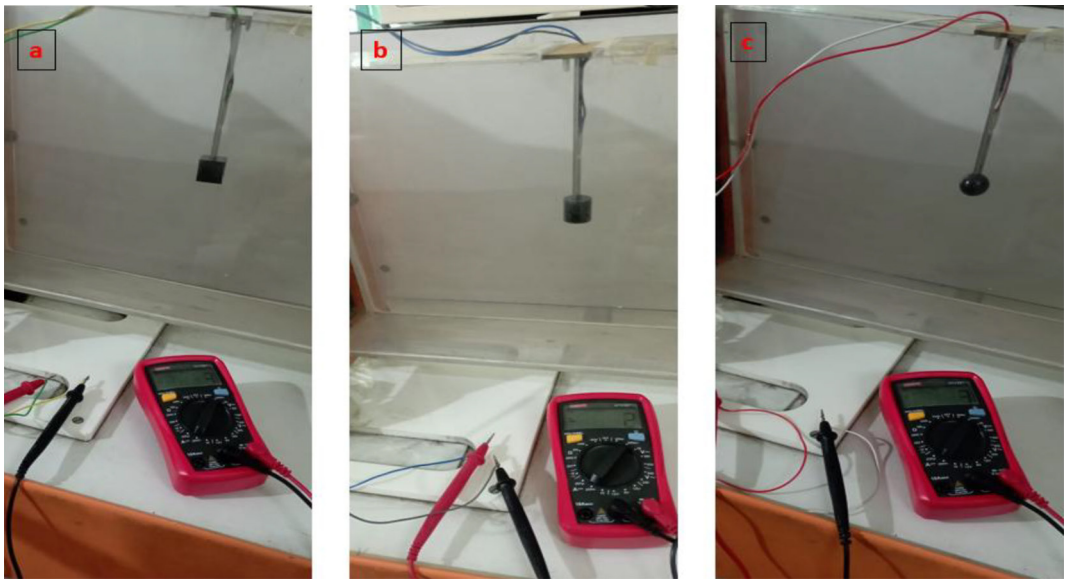

Figure 20. Experimental setups: (a) mast with cube bluff body, (b) mast with cylindrical bluff body, and (c) mast with spherical bluff body

sphere produces very weak aerodynamic excitation. Possible contributors include unmodeled turbulence in the wind tunnel, compliance in the adhesive bonding layer, and additional structural or aerodynamic damping in the experimental setup. These factors can reduce strain transmission to the piezoelectric transducer, which disproportionately affects the sphere due to its already low forcing levels.

Comparison between experimental and ANSYS results

Analyzing the results obtained from experimentation and ANSYS for the generation of voltage shows the unique aerodynamic and structural dynamics of the three prototypes differentiated the performances. The cube prototype had the highest output, with the experimental and simulated results being 5 mV and 5.145 mV, respectively. This can be explained by the cube having sharp edges that lead to powerful vortex shedding and elevated pressure drag. The coupled aerodynamic unsteady loads produced by lift drag and edge vortex structures of the cube interacted effectively with the mast vibrational modes, most notably Mode 3, where the piezoelectric transducer was positioned. The consistent correlation of experimental and simulated results further validates the energy harvesting performance of the cube geometry. The cylinder prototype was balanced in its behavior, achieving 4 mV in experiments and 4.181 mV in simulations. The good agreement in experimental and numerical data also validated the CFD–harmonic coupling method to simulate this case. The sphere prototype, in contrast, produced the lowest voltage output in its experiments at about 3 mV, with the ANSYS prediction being 3.227 mV. The sphere prototype produced the lowest voltage because its smooth, streamlined shape generates weak and poorly defined vortex shedding, resulting in low fluctuating lift forces and minimal strain transfer to the piezoelectric layer. This reduced aerodynamic excitation explains both the lower experimental output and the underprediction observed in the numerical model. Moreover, several potential sources of experimental noise can have effect on the results, including adhesive-layer compliance, slight cable vibrations, and turbulence variations within the wind tunnel, which can particularly affect the low-voltage measurements obtained from the sphere prototype. The voltage output was also tabulated in Table 9, which compares simulated and experimental outputs.

Overall, the results established a clear performance hierarchy: cube > cylinder ≫ sphere. The graph, shown in Figure 21, compares experimental and ANSYS-simulated voltages for cube,

Table 9. Simulated vs. experimental piezoelectric voltage output

Prototype	Experimental (mV)	ANSYS (mV)
Cube	5	5.145
Cylinder	4	4.181
Sphere	3	3.227

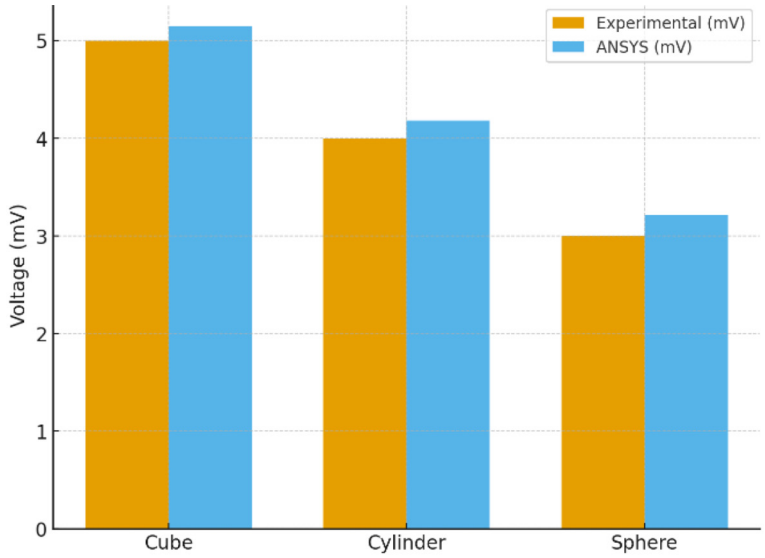

Figure 21. Comparison of experimental and ANSYS results

cylinder, and sphere geometries, showing close agreement between both results. This comparison underscored the importance of prototype geometry in optimizing piezoelectric energy harvesting under crossflow excitation.

Several peer-reviewed studies have reported experimental data for piezoelectric harvesters with cubes, cylinders, and spheres – often showing output in the low millivolt range for small devices, which is consistent with the user's results. Akaydın et al. (2010) were among the first to place piezoelectric beams in the wake of a cylinder and measured only on the order of tens of millivolts under high wind speeds [26]. In one configuration, a small PVDF piezo-film behind a 2.5 cm cylinder produced an open-circuit voltage of about 14 mV at 20.7 m/s wind speed [46] – an extremely low output, but enough to prove the VIV harvesting concept. This indicates that without resonance (or at a very small scale), the raw voltages can be quite small. Likewise, Nguyen et al. (2019) tested various mini-bluff shapes with a thin piezoelectric membrane and obtained only nanowatt power levels. Their prototype yielded under 15 mV across a load in all cases [47].

On the other hand, when resonance is achieved or when using larger piezo patches, the output increases. For a cube-shaped bluff body on a cantilever, Ewere et al. (2014) observed galloping-induced voltages of a few volts, but at relatively high wind speeds (~9–11 m/s) [48]. In the VIV regime at lower speeds, the same square prism produced much smaller voltages (0.1–0.2 V) until galloping occurred. The reported 5 mV for a cube likely corresponded to a small-scale setup in the pure vortex shedding regime, before any large amplitude galloping occurs. Such magnitudes are indeed reported in literature: for example, Bhuyan et al. (2013) built a micro-scale piezo harvester with a D-section bluff body (half-cylinder) in a 200 × 150 × 150 μm^3 channel. At a flow speed of 5 m/s, their device generated about 2.9 mV (open-circuit) from the piezoelectric cantilever [49]. This is almost exactly in the range of the user's cube result, confirming that a few millivolts is a reasonable output for a tiny piezo under those conditions.

For a cylindrical bluff body, numerous studies have documented outputs on the order of tens of millivolts up to a few volts, depending on scale. In a combined theoretical and experimental study, Abdelkefi et al. (2013) reported that a piezoelectric cylinder-harvester could reach a peak voltage of a few volts at resonance, but produced very low output (<0.1 V) off-resonance [30]. Ambrożkiewicz et al. (2022) performed wind tunnel tests on a cantilever with a 25 mm diameter cylinder and found the RMS voltage reached about 0.9 V at 5 m/s (with peaks over 1 V). However, with larger tip masses, the voltage dropped below 5 mV across the entire range [50]. This agrees with our experiment of 4 mV for a cylinder in presumably a non-optimized case – if the system's mass or damping is unfavourable, the vibrations (and hence voltage) remain very small. Notably, that study showed that increasing the cylinder's diameter from 20 mm to 25 mm raised the voltage output (due to greater aerodynamic force) and shifted the optimal speed. However, a further increase to 30 mm caused the device to stiffen and produce lower voltage overall [51]. The implication is that moderate bluff size and low damping yield the best millivolt-to-volt level response.

For the sphere, experimental data are scarcer. The omnidirectional sphere harvester by Zhang et al. (2023) demonstrated ~180–250 μW of power (with a resistive load) in the 3–8 m/s range. This corresponded to roughly 0.1 – 0.2 V across the load, assuming a mega-ohm range resistor based on the relation $P = V^2/R$ Indeed, they reported successfully powering a wireless sensor node with the device [52], implying the sphere-harvester produced on the order of a few volts AC which was then rectified – but this was achieved by an optimized spring-mass system. In a simpler configuration (sphere rigidly on a cantilever), the output would be much smaller. Encouragingly, an array or "formation" of bluff bodies can amplify the effect: a recent study on MEMS-scale harvesters showed that placing devices in a 3 × 3 grid of cylinders increased the power of the center harvester by up to 2× via constructive interference of vortices [29]. Although that study used cylinders, a similar concept could apply to spheres, where multiple spheres could influence each other's wakes.

With further optimization (e.g. using a larger piezo patch, tuning the natural frequency, or employing multiple bluff bodies), other studies have boosted outputs into the volt range [51]. For instance, an "apple-shaped" bluff body, optimized via topology methods, achieved about 8 V at 5 m/s in a lab test. Similarly, a cylinder with bio-inspired surface protrusions yielded nearly 20 V at just 2 m/s [53]. These represent state-of-the-art improvements. At the fundamental level, peer-reviewed literature confirms that simple cube,

cylinder, and sphere-based piezo harvesters can indeed generate only a few millivolts in baseline conditions. Moreover, the proposed bladeless harvester is conceptually scalable, but practical implementation would require redesigning the mast dimensions, piezoelectric area, and aerodynamic shape to maintain favourable frequency alignment at larger sizes. Scaling also demands improved power-conditioning circuits and durability assessments to ensure consistent performance under real atmospheric conditions.

LIMITATIONS

While this study provides valuable insight into how bluff-body geometry affects the performance of a bladeless piezoelectric wind harvester, several limitations should be acknowledged. The CFD simulations were performed using a steady-state RANS model, which cannot fully capture the unsteady nature of vortex shedding and may smooth out fluctuations that influence vibration strength. Additionally, the experimental work was conducted at only one wind speed because the wind tunnel available at the university operates at a fixed velocity setting; although this ensured consistent testing, it prevented exploration of resonance shifts, lock-in behaviour, or performance under varying flow conditions. The millivolt-level voltage outputs were also sensitive to small uncertainties such as cable movement or adhesive flexibility, which may have introduced minor variations in measurement. Moreover, The CFD–FEA approach assumes idealized flow conditions, perfect structural bonding, and linear material behavior, which do not fully capture real-world effects such as turbulence fluctuations, adhesive compliance, mounting imperfections, and nonlinear damping.

CONCLUSIONS

This work explored the potential of a bladeless wind energy harvester that utilizes piezoelectric transduction to convert aerodynamic forces into electrical energy. Three bluff body geometries – cube, cylinder, and sphere – were analyzed through a combination of CFD, FEA, and wind tunnel experiments. Among the prototypes, the cube configuration delivered the highest voltage output (~5 mV), followed by the cylinder (~4 mV) and the sphere (~3 mV). The cube's sharp geometry induced stronger aerodynamic loading, enhancing structural response and improving energy conversion. In contrast, the sphere exhibited reduced drag and consequently the lowest voltage output. The close agreement between numerical simulations and experimental measurements confirmed the reliability of the coupled CFD–FEA methodology. Overall, the study established the feasibility of bladeless wind harvesters and emphasizes the critical role of bluff body geometry in optimizing aerodynamic forcing, structural dynamics, and power generation.

Future work can expand on this study in several directions. Since the current wind tunnel operates at a fixed speed, conducting experiments in facilities with variable-speed capability would allow a fuller investigation of resonance, lock-in behaviour, and performance across different flow regimes. Complementing this with time-dependent CFD approaches such as URANS or LES would provide a more realistic picture of vortex shedding and fluctuating aerodynamic forces than the steady-state model used here. Incorporating frequency-domain measurements and improved turbulence models would also deepen understanding of device behaviour. Finally, investigating long-term stability, fatigue, and environmental effects would help move the bladeless piezoelectric wind harvester closer to practical and durable real-world deployment.

Acknowledgements

The authors formally acknowledge the computational and experimental support provided by the Mechanical Engineering Department (UET Lahore) for this simulation and lab testing work.

REFERENCES

1. Kang, H., et al., A novel small-scale bladeless wind turbine using vortex-induced vibration and a discrete resonance-shifting module. Applied Sciences, 2024. https://doi.org/10.3390/app14188217
2. Eldawy, R., Ghorab, A. and Sayed, M. A state-of-the-art review on vortex induced vibrations phenomenon bladeless wind turbine technology. Journal of Scientific Research and Reports, 2024. https://doi.org/10.9734/jsrr/2024/v30i112631
3. Tandel, R., Shah, S. and Tripathi, S. A state-of-art review on bladeless wind turbine. Journal of

Physics: Conference Series, 2021. 1950. https://doi.org/10.1088/1742-6596/1950/1/012058

4. Bahadur, I., Dynamic modeling and investigation of a tunable vortex bladeless wind turbine. Energies, 2022. https://doi.org/10.3390/en15186773
5. Al-Obiedy, A.N. and Al-Helli, A.H. A review of the state-of-the-art in improving piezoelectric properties. Advances in Science and Technology Research Journal, 2025; 19(6): 41–69. https://doi.org/10.12913/22998624/202784
6. Mahapatra, S., et al., Piezoelectric materials for energy harvesting and sensing applications: Roadmap for future smart materials. Advanced Science, 2021. 8. https://doi.org/10.1002/advs.202100864
7. Xiao, Y., Karnaoukh, S. and Wu, N. Design and analysis of a d15 mode piezoelectric energy generator using friction-induced vibration. Smart Materials and Structures, 2023. 32. https://doi.org/10.1088/1361-665X/acbcb1
8. Chen, B., et al., Flexible piezoelectrics: integration of sensing, actuating and energy harvesting. npj Flexible Electronics, 2025; 9(1): 58. https://doi.org/10.1038/s41528-025-00432-5
9. Sezer, N. and Koç, M. A comprehensive review on the state-of-the-art of piezoelectric energy harvesting. Nano energy, 2021; 80: 105567. https://doi.org/10.1016/j.nanoen.2020.105567
10. Jakšić, O. and Jakšić, Z. New and Emerging Materials for MEMS/NEMS: Properties and Characterization, in Micro-and Nano-Systems in 21st-Century: Designs, Developments, Applications and Perspective. Springer. 2025; 265–308.
11. Liu, J., et al., Piezoelectric thin films and their applications in MEMS: A review. Journal of Applied Physics, 2025; 137(2). https://doi.org/10.1063/5.0244749
12. Pachkawade, V., Bioinspired micro-electromechanical systems/nano-electromechanical systems: an overview, applications, and perspective. Nature-Derived Sensors, 2025; 267–293. https://doi.org/10.1016/B978-0-443-22002-9.00011-7
13. Al-Obiedy, A.N. and Al-Helli, A.H. A review of the state-of-the-art in improving piezoelectric properties. Advances in Science and Technology. Research Journal, 2025; 19(6): 41–69. https://doi.org/10.12913/22998624/202784
14. Lin, Y., et al., Progress in high-performance stick-slip piezoelectric actuators: a review. International Journal of Smart and Nano Materials, 2024; 15(3): 652–696. https://doi.org/10.1080/19475411.2024.2395293
15. Liseli, J.B., et al., An overview of piezoelectric self-sensing actuation for nanopositioning applications: Electrical circuits, displacement, and force estimation. IEEE Transactions on Instrumentation and Measurement, 2019; 69(1): 2–14. https://doi.org/10.1109/TIM.2019.2950760
16. Welburn, L., et al., Prospects and trends in biomedical microelectromechanical systems (MEMS) devices: A review. Biomolecules, 2025; 15(6): 898. https://doi.org/10.3390/biom15060898
17. Berry, D., et al., Progressing towards high performance non-resonant piezoelectric stepping actuators. Sensors and Actuators A: Physical, 2023; 358: 114439. https://doi.org/10.1016/j.sna.2023.114439
18. Adendorff, K., et al., A hybrid piezoelectric micropower generator for use in low power applications. Renewable and Sustainable Energy Reviews, 2015; 49: 1136–1144. https://doi.org/10.1016/j.rser.2015.04.143
19. Alrashdan, M.H., Hamzah, A.A. and Majlis, B.Y. Power density optimization for MEMS piezoelectric micro power generator below 100 Hz applications. Microsystem Technologies, 2018; 24(4): 2071–2084. https://doi.org/10.1007/s00542-017-3608-1
20. Wang, Z., et al., Perspective on development of piezoelectric micro-power generators. Nanoenergy Advances, 2023; 3(2): 73–100. https://doi.org/10.3390/nanoenergyadv3020005
21. Iannacci, J., Microsystem based energy harvesting (EH-MEMS): Powering pervasivity of the internet of things (IoT)–A review with focus on mechanical vibrations. Journal of King Saud University-Science, 2019; 31(1): 66–74. https://doi.org/10.1016/j.jksus.2017.05.019
22. Saadon, S. and Sidek, O. Micro-electro-mechanical system (MEMS)-based piezoelectric energy harvester for ambient vibrations. Procedia-Social and Behavioral Sciences, 2015; 195: 2353–2362. https://doi.org/10.1016/j.sbspro.2015.06.198
23. Todaro, M.T., et al., Piezoelectric MEMS vibrational energy harvesters: Advances and outlook. Microelectronic Engineering, 2017; 183: 23–36. https://doi.org/10.1016/j.mee.2017.10.005
24. Wakshume, D.G. and Płaczek, M.Ł. Optimizing piezoelectric energy harvesting from mechanical vibration for electrical efficiency: A comprehensive review. Electronics, 2024; 13(5): 987. https://doi.org/10.3390/electronics13050987
25. Sarpkaya, T., A critical review of the intrinsic nature of vortex-induced vibrations. Journal of fluids and structures, 2004; 19(4): 389–447. https://doi.org/10.1016/j.jfluidstructs.2004.02.005
26. Akaydın, H., Elvin, N. and Andreopoulos, Y. Wake of a cylinder: a paradigm for energy harvesting with piezoelectric materials. Experiments in Fluids, 2010; 49(1): 291–304. https://doi.org/10.1007/s00348-010-0871-7
27. Akaydin, H.D., Elvin, N. and Andreopoulos, Y. The performance of a self-excited fluidic energy harvester. Smart materials and Structures, 2012; 21(2): 025007. https://doi.org/10.1088/0964-1726/21/2/025007
28. Abdelkefi, A., Aeroelastic energy harvesting: A review. International Journal of Engineering Science,

2016; 100: 112–135. https://doi.org/10.1016/j.ijengsci.2015.10.006

29. Lee, Y.J., et al., Vortex-induced vibration wind energy harvesting by piezoelectric MEMS device in formation. Scientific reports, 2019; 9(1): 20404. https://doi.org/10.1038/s41598-019-56786-0
30. Abdelkefi, A., Hajj, M. and Nayfeh, A. Piezoelectric energy harvesting from transverse galloping of bluff bodies. Smart Materials and Structures, 2012; 22(1): 015014. https://doi.org/10.1088/0964-1726/22/1/015014
31. Ambrożkiewicz, B., et al., Performance analysis of a piezoelectric energy harvesting system. Advances in Science and Technology Research Journal, 2022; 16(6): 179–185.
32. Masana, R. and Daqaq, M.F. Relative performance of a vibratory energy harvester in mono-and bi-stable potentials. Journal of Sound and Vibration, 2011; 330(24): 6036–6052. https://doi.org/10.1016/j.jsv.2011.07.031
33. Naseer, R., et al., Comparative study of piezoelectric vortex-induced vibration-based energy harvesters with multi-stability characteristics. Energies, 2019; 13(1): 71. https://doi.org/10.3390/en13010071
34. Dai, H.L., et al., Orientation of bluff body for designing efficient energy harvesters from vortex-induced vibrations. Applied Physics Letters, 2016; 108(5). https://doi.org/10.1063/1.4941546
35. Li, T. and Ishihara, T. Numerical study on wake galloping of tandem circular cylinders considering the effects of mass and spacing ratios. Journal of Wind Engineering and Industrial Aerodynamics, 2021; 210: 104536. https://doi.org/10.1016/j.jweia.2021.104536
36. Abdelrheem, A., El-Helloty, A. and Ehab, A. Integrated FEM, CFD, and BIM approaches for optimizing pre-stressed concrete wind turbine tower design. Civil Engineering Journal, 2025. https://doi.org/10.28991/cej-2025-011-02-08
37. Syed, F.H., et al., A comparative study of material and structural configurations in piezoelectric energy harvesting. Emerging Science Journal, 2025. https://doi.org/10.28991/esj-2025-09-01-019
38. Prasetyo, A., et al., The effect of additional baffle plates on double-stage gravitational water vortex turbine. Civil Engineering Journal, 2025. https://doi.org/10.28991/cej-2025-011-02-011
39. Chang-Gui, Q., Computational domain setting about numerical wind tunnel in the simulation of the low-rise housing in the mountain terrain. Journal of Huaqiao University, 2010.
40. Abu-Zidan, Y., P. Mendis, and T. Gunawardena, Optimising the computational domain size in CFD simulations of tall buildings. Heliyon, 2021; 7. https://doi.org/10.1016/j.heliyon.2021.e06723
41. Ling-Lin, S., Computational domain setting for simulation of low portal framed workshops in numerical wind tunnel. Journal of Lanzhou University of Technology, 2008.
42. Younis, B.A. and V.P. Przulj, Computation of turbulent vortex shedding. Computational Mechanics, 2006; 37(5): 408–425.
43. Sarwar, W. and F. Mellibovsky, Characterization of three-dimensional vortical structures in the wake past a circular cylinder in the transitional regime. Physics of Fluids, 2020. https://doi.org/10.1063/5.0011311
44. Gerrard, J., Experimental investigation of separated boundary layer undergoing transition to turbulence. Physics of Fluids, 1967. 10. https://doi.org/10.1063/1.1762514
45. Ajitsaria, J., et al., Modeling and analysis of a bimorph piezoelectric cantilever beam for voltagegeneration. Smart Materials and Structures, 2007; 16(2): 447. https://doi.org/10.1088/0964-1726/16/2/024
46. Wang, J., J. Ran, and Z. Zhang, Energy harvester based on the synchronization phenomenon of a circular cylinder. Mathematical Problems in Engineering, 2014; 2014(1): 567357. https://doi.org/10.1155/2014/567357
47. Nguyen, H.-D.T., H.-T. Pham, and D.-A. Wang, A miniature pneumatic energy generator using Kármán vortex street. Journal of Wind Engineering and Industrial Aerodynamics, 2013; 116: 40–48. https://doi.org/10.1016/j.jweia.2013.03.002
48. Ewere, F., G. Wang, and B. Cain, Experimental investigation of galloping piezoelectric energy harvesters with square bluff bodies. Smart Materials and Structures, 2014; 23(10): 104012. https://doi.org/10.1088/0964-1726/23/10/104012
49. Bhuyan, M., et al., Development of a fluid actuated piezoelectric micro energy harvester: Finite element modeling simulation and analysis. Asian Journal of Scientific Research, 2013; 6(4): 691. https://doi.org/10.3923/ajsr.2013.691.702
50. Ambrożkiewicz, B., et al., Performance assessment of a piezoelectric vibration energy harvester for hybrid excitation with varying cross sections. Sensors, 2024; 24(23): 7629. https://doi.org/10.3390/s24237629
51. Karpiński, P., et al., Performance analysis of piezoelectric energy harvesting system under varying bluff body masses and diameters—experimental study and validation with 0–1 test. Applied Sciences, 2025; 15(13): 6972. https://doi.org/10.3390/app15136972
52. Zhang, L., et al., Omnidirectional wind piezoelectric energy harvesting. Journal of Physics D: Applied Physics, 2023; 56(23): 234003. https://doi.org/10.1088/1361-6463/acc5f4
53. Du, W., et al., Enhancing piezoelectric energy harvesting from the flow-induced vibration of an apple-shaped bluff body based on topology optimization. Energy, 2024; 307: 132667. https://doi.org/10.1016/j.energy.2024.132667